Reversible and Rapid Calcium Intercalation into Molybdenum Vanadium Oxides

Aniruddha S. Lakhnot
Rensselaer Polytechnic Institute
Kevin Bhimani
Rensselaer Polytechnic Institute
Varad Mahajani
Rensselaer Polytechnic Institute
Reena A. Panchal
Rensselaer Polytechnic Institute
Shyam Sharma
Rensselaer Polytechnic Institute
Nikhil Koratkar (koratn@rpi.edu)
Rensselaer Polytechnic Institute

Research Article

Keywords: Aqueous Ca-ion battery, POM derived oxides, Heptagonal channels, High cap. & rate performance

Posted Date: February 9th, 2022

DOI: https://doi.org/10.21203/rs.3.rs-1340697/v1

Version of Record: A version of this preprint was published at Proceedings of the National Academy of Sciences on June 21st, 2022. See the published version at https://doi.org/10.1073/pnas.2205762119.

Reversible and Rapid Calcium Intercalation into Molybdenum Vanadium Oxides

Aniruddha S. Lakhnot[1], Kevin Bhimani[1], Varad Mahajani[2], Reena A. Panchal[1], Shyam Sharma[1] and Nikhil Koratkar[1,2,#]

[1]Department of Mechanical, Aerospace and Nuclear Engineering, Rensselaer Polytechnic Institute, 110 8th Street, Troy, NY, 12180, USA.

[2]Department of Materials Science and Engineering, Rensselaer Polytechnic Institute, 110 8th Street, Troy, NY, 12180, USA.

[#]Correspondence to be addressed to N.K. (koratn@rpi.edu)

Abstract

Looming concerns regarding scarcity, high prices and safety threatens the long-term use of lithium in energy storage devices. Calcium has been explored in batteries because of its abundance and low-cost, but the larger size and higher charge density of calcium-ions relative to lithium impairs diffusion kinetics and cyclic stability. In this work, an aqueous calcium-ion battery is demonstrated using orthorhombic, trigonal and tetragonal polymorphs of molybdenum vanadium oxide (MoVO) as a host for calcium ions. Orthorhombic and trigonal MoVO outperforms the tetragonal structure because large hexagonal and heptagonal tunnels are ubiquitous in such crystals, providing facile pathways for calcium diffusion. For trigonal MoVO, a specific capacity of ~203 mAh g^{-1} was obtained at ~0.2C and at 100 times faster rate of ~20C, ~60 mAh g^{-1} capacity was achieved. The open-tunnel trigonal and orthorhombic polymorphs also promote cyclic stability and reversibility, showing a capacity fade rate of ~0.15% per cycle. A review of the literature indicates that MoVO provides one of the best performances reported to date for the storage of calcium.

Introduction

The pervasive impact of lithium (Li)-ion batteries from portable electronics to grid and renewable energy storage is indisputable.[1-4] The recent boom in electric vehicle industries also demands for high performance, affordable and safer batteries.[3] Li-ion batteries have dominated the rechargeable battery market, but the scarcity of Li resources is leading to cost and availability concerns.[5,6] To make affordable and sustainable batteries, earth-abundant metals such as Sodium (Na), Potassium (K), Magnesium (Mg), Calcium (Ca) and Aluminum (Al) are preferred.[7-13] Among these Mg, Ca and Al metal ions are multivalent in nature, i.e., one ion insertion will deliver 2 or more electrons per ion during battery operation, which boosts the specific capacity above that of alkali metal based alternatives to Li such as Na and K.[9,14,15] Consequently, multivalent ion chemistries have seen increased interest within the academic and industrial battery community. However, ions such as Mg^{2+} and Al^{3+} exhibit high charge density and therefore, strongly interact with host ions in the electrode, causing slow solid-state diffusion.[16-19] This problem is alleviated to some extent for calcium − bigger ionic size of Ca^{2+} enables lower charge density, and hence it is relatively easier for Ca^{2+} to diffuse within intercalation electrodes.[20-23] Besides this, the reduction potential of Ca^{2+} (-2.87 V vs the Standard Hydrogen Electrode) is the lowest compared to other candidate multivalent ions, which translates to higher cell voltage and energy density.[21,24]

While Ca^{2+} is easier to intercalate than Mg^{2+} and Al^{3+}, it still remains a major challenge to find a high-performing electrode host for Ca^{2+}, both due to its large size, and substantial coulombic interaction between incoming Ca-ions and host atoms within the electrode. Prussian blue analogues have been used as a host for Ca^{2+} because of their large pore sizes.[25-30] Layered materials such as V_2O_5[31] and potassium birnessite[32] have also been examined because of large spacing between 2-D layers in these materials. Recently, NASICON structured materials ($NaV_2(PO_4)_3$[33,34], $Ca_xNa_{0.5}VPO_{4.8}F_{0.7}$[35]) have been explored for Ca storage, because the ionic size of Na is very close to that of Ca (~1 Å). However, the aforementioned materials either lack high specific capacity, high-rate performance, or cyclic stability. One class of materials that have yet to be explored for Ca-ion intercalation are open-tunnel transition metal oxide structures[36] (such

as Molybdenum Vanadium Oxide (MoVO)) that contain large pores and channels for ion-transport. Such materials can be synthesized by polyoxometalate (POM) based chemistry. POMs are large metal oxyanion building blocks and by controlling reaction conditions (e.g., pH, temperature, pressure), open-channel crystals can be obtained.[37-39] For example, Sadakane et al.[37] and Ishikawa et al.[38] have synthesized five different phases of MoVO, namely Orthorhombic, Trigonal, Tetragonal, ε-Keggin POM and amorphous by tuning reaction conditions. While MoVO synthesis by traditional hydrothermal reaction methods is a time-consuming process, in a recent advance, Kaveevivitchai et al. have used microwave synthesis to drastically reduce the reaction time from 48 hours to about 1 hour.[40]

It is to be noted that choice of the electrolyte also strongly influences the performance of a Ca-ion battery.[41] Deploying Ca metal in an organic electrolyte is problematic because an ion-insulating layer forms at the metal/electrolyte interface.[13] In a recent breakthrough, reversible Ca plating/stripping was achieved, but the operational temperature was ~100 ^{o}C, and the coulombic efficiency was low.[24] Besides coulombic efficiency and cyclic stability, high-rate capability is also a challenge with organic electrolytes. Organic electrolytes contain relatively large solvent molecules, and hence incoming ions must be de-solvated prior to insertion, which slows down the kinetics.[42,43] Recent work indicates that the cyclic stability and rate performance of Ca-ion batteries can be improved by use of electrolytes containing some amount of water[25,44,45] or completely water-based (aqueous) electrolytes.[46] Water molecules need not be de-solvated and can insert along with the solvation sheath of the ion. The presence of water also shields the ionic charge, providing reduced interaction between incoming ions and the host[25,44-47]. The use of aqueous chemistries also eliminates fire hazard, which is an ever-present danger with flammable organic electrolytes.

In this study, we examined the intercalation of Ca into three different polymorphs of MoVO – Orthorhombic (Ortho), Trigonal (Tri) and Tetragonal (Tetra). The study was performed with an aqueous electrolyte containing ~5m calcium triflate. Triflate salts have high solubility in water, and large salt concentration helps to widen the electrochemical stability window, allowing higher voltages to be applied.[48-50] Ortho and Tri MoVO compounds contain 6 and 7-membered rings which are 5-6 Å wide (about

5 times bigger than a Ca ion). Typically, the hydrated radii of multivalent ions vary between 4-5 Å[20]. This can allow hydrated Ca ions to get inserted in the wide-open channels of the crystal. Both Ortho and Tri polymorphs demonstrated similar performance, but Tetra showed rapid capacity decline and reduced coulombic efficiency because of low tunnel size and irreversible loss of calcium. For Tri MoVO, the specific capacity at 0.2C was ~203 mAh g^{-1} and at rate as high as 20C, ~60 mAh g^{-1} was achieved. The open structure also promotes improved cyclic stability, demonstrating a capacity fade of ~0.15% per cycle. To gain deeper insight into rate performance, the diffusion of Ca^{2+} in Tri MoVO was characterized using CV, EIS and GITT methods. The measured Ca^{2+} diffusion coefficients are orders of magnitude faster than that of multivalent ions such as Mg^{2+}, and even faster than Li^{+} diffusion into typical oxide based electrodes. Ex-situ XPS and XRD confirmed the reversibility of Ca^{2+}intercalation, and the structural stability of Ortho and Tri phases of MoVO. These results showcase the potential of developing open-tunnel transition metal oxide structures, to build superior performing Ca-ion batteries.

Results

Materials Synthesis and Characterization

A schematic of the synthesis process for Ortho MoVO has been shown in **Fig. 1a**. Ammonium molybdate and vanadyl sulfate were used as the precursor source for Mo and V respectively. Solutions were mixed under N_2 atmosphere to avoid excess oxygen. The mixed solution was acidic (pH ~ 3) because the molecules present in the solution belong to a class of compounds called polyoxometalates (POMs). POMs are metal-oxo cluster anions which acts as building units (B.U.) for structural transformation. Final structure is defined by the arrangements of B.U. and octahedra linkers, which can be tuned by process parameters such as pH, time, temperature, and pressure. In the present case, Mo_6O_{21} is the B.U. (**Supplementary Fig.1**) and the reaction conditions (as described in **Fig. 1**), generates Ortho MoVO. Tri MoVO was obtained by changing pH of the mixed solution to ~2.2 and Tetra MoVO was derived from Ortho MoVO by thermal transformation (heated at ~575 ^{0}C for 2 hrs. under N_2). The XRD data in **Fig. 1b** confirms the formation of

the desired compounds based on the literature[51]. **Figure 1c-e** shows the crystal structure of Ortho, Tri and Tetra MoVO respectively. Both the Ortho and Tri structure contains heptagonal as well as hexagonal voids. These are big micropores (in the 5-6 Å range), which can accommodate large cations (e.g. Ca^{2+}) and small molecules. Tetra on the other hand is limited to much smaller pentagonal, tetragonal and trigonal voids. FTIR spectrum (**Supplementary Fig. 1**) of all three MoVO polymorphs is almost identical indicating that bonding states and building units are same, and it is only the arrangement of building units which give rise to different crystal structures. Morphology of the samples were examined under SEM (**Fig. 1f-h**). MoVO oxides are long rods (4 – 10 µm) ranging from 400 – 700 nm in diameter. Inset figures show EDS mapping which demonstrates uniform distribution of Mo, V and O elements in the rods. **Figure 1i** is a typical EDS spectrum of Tri MoVO. Multiple samples were characterized to establish its' molecular formula, which was estimated as $Mo_{2.5+y}VO_{10+z}$ ($0<y\leq 0.5$; $0<z\leq 1$); Ortho and Tetra phases showed similar stoichiometry.

Electrochemical Properties

Electrochemical tests were performed on a custom built cell (**Supplementary Fig. 2**) and activated carbon (AC) was used as a pseudo reference electrode. Activated carbon was calibrated (**Supplementary Fig. 3**) and it exhibits a potential of 3.247 V vs Ca^{2+}/Ca. The samples were cycled within the electrochemical stability window **(Supplementary Fig. 4**) of 5m $Ca(OTf)_2$ aqueous electrolyte. **Figure 2a-c** represents cyclic voltammograms (CV) of Ortho, Tri and Tetra MoVO conducted at 0.1 mV s^{-1}. The CV profile was quite similar for Ortho and Tri. One notable feature in all CV curves was that the current peak (in the range -0.98 to -1.2 V) during first discharge, vanished after the third cycle. This peak is attributable to SEI formation. One broad peak at around -0.51 V and another at -1.4 V was observed during discharge for both Ortho and Tri MoVO (**Fig. 2a-b**). Three pair of anodic peaks at -0.27, -0.37 and -1.2 V for Ortho and -0.26, -0.48 and -1.21 V for Tri were also observed. We believe that the initial broad peak (at -0.51 V) and corresponding anodic peaks (-0.26 and -0.48 V) occur because of vanadium taking part in the redox process. This aligns well with vanadium-based cathodes employed in Ca-ion batteries.[31,52] As will be discussed in later sections, the peak at -1.4 V / -1.2 V could be attributed to a mix of both redox process as well as

capacitive mechanism participating in the charge storage process. CV profiles overlap well after the third cycle suggesting good reversibility. For Tetra MoVO (**Fig. 2c**), peaks at deeper discharge (-1.2 to -1.4 V) were not detected, which indicates its' lower electrochemical activity. Tetra has much smaller size voids in the structure, which limits capacitive storage as well as Ca-ion intercalation. Moreover, the CV curves for Tetra do not overlap well even at the 5th cycle, indicating the irreversible nature of this material.

To further investigate the voltage profile and cyclic stability, batteries were tested using galvanostatic cycling at 100 mA g^{-1} (**Fig. 2d-f**). The first cycle voltage profile was very different compared to the rest of the cycles, which corroborates the CV results and is attributed to SEI formation. The discharge voltage plateaus at -0.4 V and -1.2 V are evident in the case of Ortho and Tri (**Fig. 2d-e**). Voltage profiles were repeatable and sustained through to the 100th cycle. Both materials show reversible specific capacity of ~165 mAh g^{-1} during initial cycles and retained to ~140 mAh g^{-1} at the end of the 100th cycle. These results reveal the stable and reversible performance of Ortho and Tri MoVO. For Tetra (**Fig. 2f**), the profile was not repeatable, and it degraded drastically during the initial 10 cycles (drops from 120 to 78 mAh g^{-1}) but stabilized in later cycles. The 50th and 100th cycle have similar voltage profile, delivering a reversible capacity of ~46 mAh g^{-1}. These data indicate that Tetra MoVO exhibits irreversible capacity in the initial cycles. This is presumably due to the smaller void size of Tetra MoVO, making it challenging for Ca-ions to reversibly diffuse in and out of the structure. The cyclic stability of all three materials has been compared in **Fig. 2g-h**. For Ortho and Tri, there is a slight increment in initial capacity which could be because of electrode activation (**Fig. 2g**). For Ortho, the specific capacity drops from ~165 mAh g^{-1} to ~144 mAh g^{-1}, displaying a capacity retention of ~87% at the end of 100 cycles, whereas Tri drops from ~163 mAh g^{-1} to ~138 mAh g^{-1} with a capacity retention of ~85%. Nonetheless, the performance is similar for Ortho and Tri. In case of Tetra (**Fig. 2g**), the specific capacity drastically drops from 120 mAh g^{-1} to 46 mAh g^{-1} over the first 35 cycles and then it remains stable till the 100th cycle. The reason for its poor performance is evident when coulombic efficiency is compared in **Fig. 2h**. In just 2 cycles, coulombic efficiency has jumped from 84% to 96% for Ortho and from 88% to 97% for Tri, but when Tetra is observed, it took 63

cycles to improve from 54% to 95%. This is a clear indication of high irreversibility in Tetra MoVO. Multivalent ions generally find it difficult to migrate through the crystal structure because of their high charge density. When these ions encounter a relatively condensed space (as in Tetra MoVO), they are more likely to interact with the host atoms present in the electrode, resulting in a strenuous de-insertion process, which leads to higher irreversibility.

Once the low-rate cyclic stability of Ortho and Tri was confirmed, we proceeded to test their rate capability. **Figure 2i** shows the rate capability performance of Tri MoVO. A specific capacity of ~203 mAh g^{-1} was obtained at 0.2 C (1C = 150 mA g^{-1}) which slowly degrades with rate. Specific capacities of ~113 mAh g^{-1}, ~89 mAh $g^{-1}$and ~61 mAh g^{-1} were obtained at C-rates of 5C, 10C and 20C respectively. Similar results for high-rate performance were also demonstrated by Ortho (**Supplementary Fig. 5**). These rate performances are among the highest reported for Ca-ion battery systems. The reason for this outcome is presumably due to the large size and open tunnels available in the crystal structure, enabling facile diffusion of ions. Further, since we are utilizing an aqueous chemistry, ions along with its solvation sheath can get inserted. The solvated ions shield the ionic charge, reducing coulombic interaction and hence facilitating faster diffusion in the host. Another factor that could aid rapid Ca^{2+} intercalation and de-intercalation is that the transition metals (i.e., Mo and V) in MoVO have variable oxidation states, and can get reduced to lower oxidation states during Ca^{2+} insertion. This allows for easy charge redistribution, which can help maintain uniform charge neutrality in the material.

Ex-Situ Study of Cycled Electrodes

To verify that it is Ca inserting in the material (sometimes protons present in aqueous electrolytes can start participating in the electrochemical reaction), EDS mapping and EDS spectrum (**Fig. 3a-b**) of cycled Tri MoVO were acquired. Uniform distribution of Ca is noticeable, and peaks of Ca are visible in the spectrum. Similar records were acquired for Ortho and Tetra MoVO (**Supplementary Fig. 6**). To verify reversibility of calcium insertion, samples at various discharge states were analyzed under XPS (**Fig. 3c**). In the pristine electrode, Ca 2p peaks are obviously “absent”, and it starts to appear at -0.4 V. The peak

becomes very intense at the maximum discharge state of -1.4 V. When the cell was charged back to 0.3 V, the Ca peak almost disappears, which verifies the reversible extraction of Ca. The robustness of the MoVO crystal structure was checked by XRD on electrodes after 100 electrochemical cycles (**Fig. 3d**). The XRD profile remains same for all three polymorphs of MoVO (**Supplementary Fig. 7**). This substantiates the extreme structural integrity of MoVO compounds, which contributes to their stable cycling performance. SEM imaging of the cycled electrodes (**Supplementary Fig. 8**) attest to the fact that the electrode structure remains intact during the cycling process.

Kinetic Study of Ca in MoVO Electrode

To further investigate the high-rate performance of Tri MoVO, we studied its kinetic behavior by determining the Ca^{2+} diffusion coefficient. For an initial estimation, the diffusion coefficient was calculated using the Randles-Sevcik equation[53-57]:

$$i_p = (2.69 \times 10^5)\, n^{3/2} A D_{Ca}^{1/2} C \nu^{1/2} \quad (1)$$

Where I_p is peak current in the CV curve, n is the charge transfer number, A is surface area of electrode, D_{Ca} is the diffusion coefficient of Ca, C is concentration of Ca in the MoVO electrode and ν is the scan rate. To use equation (1), CV was performed at different scan rates as shown in **Fig. 4a**. D_{Ca} for a purely diffusive process can be extracted by performing a linear fit to the peak current vs the (scan rate)$^{0.5}$ plot. **Figure 4b** is the plot of peak current vs (scan rate)$^{0.5}$ at -0.51 V for the discharge process, and at -0.27 V for the charge process. During discharge, D_{Ca} was estimated as 1.07×10^{-10} cm^2 s^{-1} and during charge D_{Ca} was 3.2×10^{-10} cm^2 s^{-1}. A similar calculation could not be carried out for the current peak at -1.22 V, since the peak current did not exhibit a linear correlation with (scan rate)$^{0.5}$, rather, the relation could be best fitted by utilizing a power law equation[32,52,58,59]:

$$i_p = a\nu^b \quad (2)$$

Note that a value of 0.5 for b indicates a purely diffusive process, while b value of 1 indicates a purely capacitive mechanism. In **Fig. 4c**, 'b' is 0.77 for the peak current at -1.22 V, which indicates that at this voltage, the storage mechanism in MoVO is a mix of both diffusive and capacitive behavior.

To further determine diffusion coefficient at different voltage values, Electrochemical Impedance Spectroscopy (EIS) was performed at OCV, -0.4 V, -1.0 V and -1.4 V during the discharge process. **Figure 4d** presents the EIS spectrum of Tri MoVO at various voltage values and the data was fit by the circuit model described in the inset. For the Nyquist plot, in the high frequency region, the intercept on Z' -axis corresponds to solution resistance (R_s) and contact resistance of the cell, and the semi-circle can be ascribed to the charge transfer (R_{ct}) and SEI impedance of the electrodes. A small net resistance of < 9 Ω was registered at all the voltage values, which promotes facile operation of the battery at high C-rates. The oblique feature at the end in the low frequency regime is associated with the Warburg impedance, which is related to Ca-ion diffusion in the electrode material. To calculate the diffusion coefficient, equations (3) and (4) were used[52,57,60-63].

$$D_{Ca} = \frac{R^2T^2}{2A^2n^4F^4C^2\sigma^2} \quad (3)$$

$$Z' = R_s + R_{ct} + \sigma\omega^{-1/2} \quad (4)$$

Here, R is the gas constant, T is absolute temperature, A is surface area of the electrode, n is charge transfer number, F is Faraday constant, C is concentration of Ca in the material and σ is the Warburg factor. To calculate Warburg factor, equation (4) was used, which was obtained from the Z' (real) vs $\omega^{0.5}$ plot in the low frequency regime. The slope of the linear fit between Z' (real) vs $\omega^{0.5}$ will yield σ. **Figure 4e** contains the linear fit at all four voltage values. D_{Ca} at OCV is calculated to be 1.44×10^{-10} cm^2 s^{-1}, which is very close to the value calculated from CV. A similar study was performed on Ortho (**Supplementary Fig. 9**) and the D_{Ca} for Ortho is very close to what was exhibited by Tri MoVO.

Galvanostatic Intermittent Titration Technique (GITT) characterization (**Fig. 4f**) was also carried out to obtain deeper insight into the diffusion process. For this, a current pulse at 75 mA g^{-1} was applied for 15 minutes followed by 2 hrs. of relaxation time. The maximum absolute voltage during the 15 minutes period generated by the current pulse accounts for the kinetic condition. On the other hand, the minimum absolute potential achieved after 2 hrs. of relaxation, represents the equilibrium state. Both kinetic and

equilibrium conditions have been highlighted in **Fig. 4f**. The zoomed in picture of one such current, relaxation cycle at roughly -0.4 V has been provided in **Fig. 4g**. When the current pulse is applied, there is a sudden drop in voltage which could be attributed to the resistance drop, and thereafter there is a drop induced by the electrochemical reaction. This change in potential is ΔE_τ, which is regarded as the change in potential due to kinetic conditions. Subsequently, when the relaxation period starts, there is a sudden voltage rise, and then the potential slowly increases and eventually saturates at the end of 2 hrs. The difference between the saturated potential from the current cycle and the saturated potential from the previous cycle represents the voltage change in the equilibrium condition (ΔE_s). The diffusion coefficient can be calculated by using equation (5)[60,64,65]:

$$D_{Ca} = \frac{4}{\pi\tau}\left(\frac{mV_m}{mA}\right)^2\left(\frac{\Delta E_s}{\Delta E_\tau}\right)^2 \text{ for } \tau \ll \frac{L^2}{D} \quad (5)$$

Equation (5) is valid, if E_τ vs $\tau^{1/2}$ follows a linear relation, and **Fig. 4h** validates this. Hence, equation (5) was applicable for the calculation of diffusion coefficients from the GITT data. **Figure 4i** compares the diffusion coefficients retrieved from EIS and GITT experiments. Both EIS and GITT results show the same trend at different voltages, with GITT predicting relatively higher diffusion coefficients. The Ca diffusion coefficient is higher initially (i.e. at the onset of intercalation) because of a large concentration gradient at the MoVO/electrolyte interface. Subsequently, as increasing amounts of Ca-ions get inserted into the material, the concentration gradient drops. Moreover, there is reduced non-intercalated volume remaining within the structure to accommodate more incoming Ca-ions. The net result is much lower diffusivity of Ca-ions towards the end of the discharge step.

The Ca^{2+} diffusion coefficients (**Fig. 4i**) in the range 5.7×10^{-10} cm^2 s^{-1} to 2.54×10^{-14} cm^2 s^{-1} that we report are orders of magnitude faster than multivalent ions such as Mg^{2+}, which show diffusion coefficients of 10^{-16} to 10^{-19} cm^2 s^{-1} into oxide hosts such as α-MoO_3 and TiO_2.[66,67] In fact Ca^{2+} diffusion is even faster than Li-ion diffusion (10^{-14} to 10^{-16} cm^2 s^{-1}) into oxide materials such as $Nb_{18}W_{16}O_{93}$[57], H-Nb_2O_5[68], TiO_2[69]

and $Li_4Ti_5O_{12}$[70]. These results explain the ability of Ca^{2+} to intercalate effectively into Tri MoVO at fast charge/discharge rates of up to 20C (**Fig. 2i**).

Comparison with State-of-Art

We compared the performance of Tri MoVO with various Ca-ion electrode materials reported in the literature. Specific capacity comparison of the various materials at low C-rates is shown in **Fig. 5a**. The literature from which this data is taken is provided in **Supplementary Table 1**. Tri MoVO with a specific capacity of ~203 mAh g^{-1} (at 0.2C) is superior to almost all the reported materials. Calcium because of its relatively large size and high charge density induces large stresses in the host material causing structural damage. As a result, several materials lose their capacity in just a few cycles, resulting in a massive capacity fade. The capacity fade rate for various materials tested in Ca-ion batteries is summarized in **Fig. 5b**. The capacity fade rate per cycle was calculated using equation (6):

$$\text{Capacity fade rate per cycle} = \frac{(\text{Initial Capacity} - \text{Final Capacity})}{\text{Initial Capacity}} \times 100 \times \frac{1}{\text{Cycle Index}} \quad (6)$$

Tri-MoVO shows a relatively benign capacity fade rate of ~0.15% per cycle, which is much lower than a variety of materials including oxides, phosphates, polymers, and Prussian blue analogues (**Fig. 5b**). Very few studies in the literature report rate-capability in Ca-ion batteries. The available literature on rate-capability has been provided in **Fig. 5c**. Tri MoVO is among the best available materials in terms of delivering high specific capacity over a wide range of current densities. For example, it delivers a specific capacity of ~100 mA h g^{-1} at ~1000 mA g^{-1} current density. Based on the test data in **Fig. 5c**, we conclude that PT (5,7,12,14-pentacenetetrone)[71] is the only material reported to date that shows far superior rate capability than MoVO, however it should be noted that the primary charge storage mechanism for PT is capacitive rather than diffusive, and protons also contribute to charge storage in PT.[71]

Discussion

To summarize, we report high specific capacity and high-rate performing MoVO materials as a host for Ca-ion intercalation in aqueous electrolytes. Polyoxometalate derived MoVO polymorphs were prepared by hydrothermal processing. Open-crystal structured materials with heptagonal and hexagonal tunnels (orthorhombic, trigonal) as well as pentagonal tunnels (tetragonal) were employed in concentrated aqueous electrolyte (5m $Ca(OTf)_2$). Both orthorhombic (Ortho) and trigonal (Tri) demonstrated similar performance, but tetragonal (Tetra) showed rapid capacity decline and reduced coulombic efficiency because of low tunnel size and irreversible loss of Ca. For Tri MoVO, the specific capacity at a low rate of 0.2C was ~203 mAh g^{-1}, and even at a high-rate of 20C, a specific capacity of ~60 mAh g^{-1} was retained. The open structure of Tri also promotes cyclic stability, demonstrating a capacity fade of ~0.15% per cycle, which is low relative to most oxides, phosphates, polymers, and Prussian blue analogues tested in Ca-ion batteries. To gain deeper insight into the rate performance, the diffusion coefficient of Ca^{2+} was calculated using CV, EIS and GITT. At the initial stage, inside a relatively empty oxide material, a Ca diffusion coefficient of ~5.7×10^{-10} cm^2 s^{-1} was achieved, and it retains a value in excess of 10^{-12} cm^2 s^{-1} in the middle stage of the discharge cycle. These values compare favorably with multivalent ions (such as Mg^{2+}) as well as Li^+ insertion into oxide hosts. The reversible insertion and de-insertion of Ca was also confirmed by ex-situ EDS and XPS characterization. EDS mapping revealed the presence of Ca, whereas XPS analysis at various discharge states verified reversible Ca 2p peaks. These results indicate a reversible system for Ca-ion intercalation with high specific capacity and rate capability and opens new avenues for the deployment of open-crystal structured materials such as MoVO in future energy storage devices.

Methods

Materials Synthesis

For synthesis of Ortho MoVO, ~40 ml of 50 mM ammonium molybdate ($(NH_4)_6Mo_7O_{24}$, Sigma Aldrich > 99 %) was put it a round bottom flask. The solution was degassed and then N_2 gas was bubbled

through the solution with the help of a needle. Another needle was used as a vent. The solution was under vigorous stirring and under nitrogen atmosphere when ~40 ml of 12.5 mM vanadyl sulfate ($VOSO_4$, Sigma Aldrich 97%)) was injected drop-by-drop using a syringe. Dark purple solution was obtained at the end, which was left for 20 minutes under nitrogen bubbling to avoid any excess oxygen. Resulting solution was quickly transferred to a Teflon container to be placed in a hydrothermal reactor. Hydrothermal reaction was carried out at ~180 ^{0}C for 48 hrs, Afterwards, the container was left overnight to cool down in the furnace. A greyish precipitate was obtained which was separated from the solution by vacuum filtration. This filtered product was dried overnight in a vacuum oven at ~80 ^{0}C and then treated with oxalic acid (0.4M) at ~60 ^{0}C for half an hour. Oxalic acid treatment was performed to get rid of amorphous impurities. The oxalic acid treated powder was filtered and vacuum dried. In the last step of the synthesis process, the powder was heated in box furnace at ~400 ^{0}C for 4 hrs. to remove any water and ammonia molecules. This processing technique has been adopted from the literature[37,39].

Tri MoVO, was prepared through the same process as Ortho MoVO, except, pH of the dark purple solution (obtained after mixing Mo and V precursors) was adjusted to ~2.2 by dropping ~2 M H_2SO_4 solution and hydrothermal reaction time was only 20 hrs. Tetra MoVO, was derived from Ortho MoVO by heating Ortho MoVO at ~575 ^{0}C for 2 hrs. in N_2 atmosphere. The heating rate was ~10 ^{0}C/min, and the sample was left to cool down under N_2.

Electrode preparation was identical for all three oxide materials and the activated carbon (4% Ash, Thermo Scientific) electrode. Briefly, the sample, super P conductive carbon and PVDF (4wt% in NMP) were mixed in planetary mixer such that the final composition of slurry (sample: superP: PVDF) was 80:10:10 weight ratio. The slurry was then coated on titanium foil (0.25 mm, 99.99%, Thermo Scientific) for MoVO and on Al foil for activated carbon. Finally, the electrodes were left for drying overnight. Mass loading of MoVO electrodes was 2-3 mg cm^{-2} and the electrode thickness was in the range of 25-30 µm (**Supplementary Fig. 10**). Electrode density for Tri MovO was calculated to be ~0.87 g ml^{-1}. For activated carbon, free standing film was achieved due to high mass loading (80–100 mg cm^{-2}). 5m aqueous $Ca(OTf)_2$

(Calcium trifluoromethanesulfonate, 99% min, Thermo Scientific) was used as the electrolyte. To prepare the electrolyte, calcium salt was measured inside an argon filled glove box, and HPLC grade water was quickly added in the ambient.

Materials Characterization

Crystal structure of MoVO particles were confirmed by X-ray diffraction (XRD) which was performed using Panalytical X'pert PRO MPD system. Cu Kα radiation (λ = 1.54 Å) was used and 2theta range of 5^0 to 60^0 was scanned with 0.05^0 step size. Scanning electron microscopy (SEM) and energy dispersive spectroscopy (EDS) mapping was conducted on Carl Zeiss Supra 55 FESEM to examine morphology, size and elemental distribution. A Carl Zeiss 1540EsB Crossbeam system was used for scanning electron microscopy (5 kV) and focused ion beam work (Ga ion, 30 kV). X-ray photoelectron spectroscopy (XPS) was accomplished using Al Kα radiation in a PHI 5000 Versa probe system. XPS analysis was performed after Ar^+ ion sputtering for ~15 min to avoid interference from SEI or surface impurities. For ex-situ studies, the samples were cycled for 3 cycles under galvanostatic condition at ~100 mA g^{-1} and then held at a particular potential for 15 – 20 hrs. Afterwards, the cells were opened to extract the electrode, thoroughly washed with DI water, and dried for ~2 hrs. in a vacuum oven at ~80 ^{0}C.

Electrochemical Analysis

All electrochemical tests were conducted on a custom-built cell (**Supplementary Fig. 2**). Conventional coin cells could not be used because the electrolyte starts to reduce on stainless steel. Nylon/ Teflon plates were used because of their mechanical robustness and electrochemical stability. 10 sets of hex head bolts and nuts were used to tightly seal the battery. Activated carbon was used as a pseudo reference electrode. It was calibrated using $LiFePO_4$ electrode (MTI corp.). $LiFePO_4$ was first tested against Li^+/Li in 1M $LiPF_6$ in EC: DEC (1:1). An insertion potential of 3.475 V was noted against Li^+/Li. $LiFePO_4$ then was tested against AC, which demonstrated an insertion potential of 0.048 V against AC. These tests concluded that AC potential is 3.427 V vs Li^+/Li and hence 3.247 V vs Ca^{2+}/Ca.

Galvanostatic charge discharge and GITT tests were performed on Arbin BT2000 in the 0.3 to -1.4 V range. For GITT, a current pulse of 75 mA g^{-1} was applied for 15 min and rest period of 2 hrs. was given for relaxation. Voltage stability window of 5m $Ca(OTf)_2$ was determined using linear sweep voltammetry (LSV) at 1 mV s^{-1}. LSV, Cyclic voltammetry testing and EIS were performed on Gamry Reference 3000 potentiostat. For conducting EIS at a particular potential, the cell was discharged at 100 mA g^{-1} and then held at the desired potential for ~2 hrs.

References

1. Dunn, B., Kamath, H. & Tarascon, J. M. Electrical energy storage for the grid: A battery of choices. *Science* **334**, 928–935 (2011).
2. Armand, M. & Tarascon, J.M. Building better batteries. *Nature* **451**, 652-657 (2008).
3. Amine, K., Kanno, R. & Tzeng, Y. Rechargeable lithium batteries and beyond: Progress, challenges, and future directions. *MRS Bull.* **39**, 395–401 (2014).
4. Van Noorden, R. The rechargeable revolution: A better battery. *Nature* **507**, 26–28 (2014).
5. Lee, K. T., Jeong, S. & Cho, J. Roles of Surface Chemistry on Safety and Electrochemistry in Lithium Ion Batteries. *Acc. Chem. Res.* **46**, 1161–1170 (2012).
6. Komaba, S. *et al.* Electrochemical Na Insertion and Solid Electrolyte Interphase for Hard-Carbon Electrodes and Application to Na-Ion Batteries. *Adv. Funct. Mater.* **21**, 3859–3867 (2011).
7. Yabuuchi, N., Kubota, K., Dahbi, M. & Komaba, S. Research Development on Sodium-Ion Batteries. *Chem. Rev.* **114**, 11636–11682 (2014).
8. Rajagopalan, R. *et al.* Advancements and Challenges in Potassium Ion Batteries: A Comprehensive Review. *Adv. Funct. Mater.* **30**, 1909486 (2020).
9. Yoo, H. D. *et al.* Mg rechargeable batteries: an on-going challenge. *Energy Environ. Sci.* **6**, 2265–2279 (2013).
10. Elia, G. A. *et al.* An Overview and Future Perspectives of Aluminum Batteries. *Adv. Mater.* **28**, 7564–7579 (2016).
11. Muldoon, J., Bucur, C. B. & Gregory, T. Quest for Nonaqueous Multivalent Secondary Batteries: Magnesium and Beyond. *Chem. Rev.* **114**, 11683–11720 (2014).
12. Gummow, R. J., Vamvounis, G., Kannan, M. B. & He, Y. Calcium-Ion Batteries: Current State-of-the-Art and Future Perspectives. *Adv. Mater.* **30**, 1801702 (2018).
13. Ponrouch, A. & Palacin, M. R. On the road toward calcium-based batteries. *Curr. Opin. Electrochem.* **9**, 1–7 (2018).
14. Doe, R. E. *et al.* Novel, electrolyte solutions comprising fully inorganic salts with high anodic stability for rechargeable magnesium batteries. *Chem. Commun.* **50**, 243–245 (2013).

15. Muldoon, J. *et al.* Electrolyte roadblocks to a magnesium rechargeable battery. *Energy Environ. Sci.* **5**, 5941–5950 (2012).

16. Liang, Y. *et al.* Interlayer-expanded molybdenum disulfide nanocomposites for electrochemical magnesium storage. *Nano Lett.* **15**, 2194–2202 (2015).

17. Amatucci, G. G. *et al.* Investigation of Yttrium and Polyvalent Ion Intercalation into Nanocrystalline Vanadium Oxide. *J. Electrochem. Soc.* **148**, A940 (2001).

18. Levi, E., Levi, M., Chasid, O., & Aurbach, D. A review on the problems of the solid state ions diffusion in cathodes for rechargeable Mg batteries. *Electroceramics* **22**, 13-19 (2009).

19. Aurbach, D., Weissman, I., Gofer, Y. & Levi, E. Nonaqueous magnesium electrochemistry and its application in secondary batteries. *Chem. Rec.* **3**, 61–73 (2003).

20. Nightingale Jr, E.R. Phenomenological Theory of Ion Solvation. *J. Phys. Chem.* **63**, 1381-1387 (1959).

21. Gheytani, S. *et al.* An Aqueous Ca-Ion Battery. *Adv. Sci.* **4**, 1700465 (2017).

22. Tojo, T., Sugiura, Y., Inada, R. & Sakurai, Y. Reversible Calcium Ion Batteries Using a Dehydrated Prussian Blue Analogue Cathode. *Electrochim. Acta* **207**, 22–27 (2016).

23. Smeu, M. *et al.* Theoretical investigation of Chevrel phase materials for cathodes accommodating Ca2+ ions. *J. Power Sources* **306**, 431–436 (2016).

24. Ponrouch, A., Frontera, C., Bardé, F. & Palacín, M. R. Towards a calcium-based rechargeable battery. *Nat. Mater. 2015 152* **15**, 169–172 (2015).

25. Padigi, P., Goncher, G., Evans, D. & Solanki, R. Potassium barium hexacyanoferrate – A potential cathode material for rechargeable calcium ion batteries. *J. Power Sources* **273**, 460–464 (2015).

26. Lee, C. & Jeong, S. K. Modulating the hydration number of calcium ions by varying the electrolyte concentration: Electrochemical performance in a Prussian blue electrode/aqueous electrolyte system for calcium-ion batteries. *Electrochim. Acta* **265**, 430–436 (2018).

27. Kuperman, N. *et al.* High performance Prussian Blue cathode for nonaqueous Ca-ion intercalation battery. *J. Power Sources* **342**, 414–418 (2017).

28. Lipson, A. L. *et al.* Nickel hexacyanoferrate, a versatile intercalation host for divalent ions from nonaqueous electrolytes. *J. Power Sources* **325**, 646–652 (2016).

29. Shiga, T., Kondo, H., Kato, Y. & Inoue, M. Insertion of Calcium Ion into Prussian Blue Analogue in Nonaqueous Solutions and Its Application to a Rechargeable Battery with Dual Carriers. *J. Phys. Chem. C* **119**, 27946–27953 (2015).

30. Dutta, P. K., Adil, M., Dutta, K. & Mitra, S. An Aqueous Ca-ion Full Cell Comprising BaHCF Cathode and MCMB Anode. *Chem.* Select **3**, 3687-3690 (2018).

31. Murata, Y. *et al.* Effect of water in electrolyte on the Ca^{2+} insertion/extraction properties of V_2O_5. *Electrochim. Acta* **294**, 210–216 (2019).

32. Hyoung, J., Heo, J. W. & Hong, S. T. Investigation of electrochemical calcium-ion energy storage mechanism in potassium birnessite. *J. Power Sources* **390**, 127–133 (2018).

33. Kim, S. *et al.* High-Voltage Phosphate Cathodes for Rechargeable Ca-Ion Batteries. *ACS Energy Lett.* **5**, 3203–3211 (2020).

34. Jeon, B. *et al.* Reversible calcium-ion insertion in NaSICON-type $NaV_2(PO_4)_3$. *Chem. Mater.* **32**, 8772–8780 (2020).

35. Xu, Z. L. *et al.* A new high-voltage calcium intercalation host for ultra-stable and high-power calcium rechargeable batteries. *Nat. Commun. 2021 121* **12**, 1–9 (2021).

36. Qu, G. *et al.* Phase Engineering of Mo-V Oxides for Zinc-Ion Batteries. Preprint at doi:10.21203/rs.3.rs-94180/v1 (2020).

37. Sadakane, M. *et al.* Assembly of a Pentagonal Polyoxomolybdate Building Block, $[Mo_6O_{21}]_{6-}$, into Crystalline MoV Oxides. *Eur. J. Inorg. Chem.* **2013**, 1731–1736 (2013).

38. Ishikawa, S. & Ueda, W. Microporous crystalline Mo–V mixed oxides for selective oxidations. *Catal. Sci. Technol.* **6**, 617–629 (2016).

39. Konya, T. *et al.* An orthorhombic Mo_3VO_x catalyst most active for oxidative dehydrogenation of ethane among related complex metal oxides. *Catal. Sci. Technol.* **3**, 380–387 (2013).

40. Kaveevivitchai, W. *et al.* Rechargeable Aluminum-Ion Batteries Based on an Open-Tunnel Framework. *Small* **13**, 1701296 (2017).

41 Wang, M. *et al.* Reversible calcium alloying enables a practical room-temperature rechargeable calcium-ion battery with a high discharge voltage. *Nat. Chem. 2018 106* **10**, 667–672 (2018).

42. Kundu, D. *et al*. Aqueous vs. nonaqueous Zn-ion batteries: consequences of the desolvation penalty at the interface. *Energy Environ. Sci.* **11**, 881-892 (2018).

43. Wang, F. *et al.* High-Voltage Aqueous Magnesium Ion Batteries. *ACS Cent. Sci.* **3**, 1121–1128 (2017).

44. Jaehee Song *et al.* Activation of a MnO_2 cathode by water-stimulated Mg^{2+} insertion for a magnesium ion battery. *Phys. Chem. Chem. Phys.* **17**, 5256–5264 (2015).

45. Novák, P., Imhof, R. & Haas, O. Magnesium insertion electrodes for rechargeable nonaqueous batteries — a competitive alternative to lithium? *Electrochim. Acta* **45**, 351–367 (1999).

46. Guduru, R. K. & Icaza, J. C. A Brief Review on Multivalent Intercalation Batteries with Aqueous Electrolytes. *Nanomater* **6**, 41 (2016).

47. Wang, R. Y., Wessells, C. D., Huggins, R. A. & Cui, Y. Highly reversible open framework nanoscale electrodes for divalent ion batteries. *Nano Lett.* **13**, 5748–5752 (2013).

48. Suo, L. *et al.* Advanced High-Voltage Aqueous Lithium-Ion Battery Enabled by "Water-in-Bisalt" Electrolyte. *Angew. Chemie - Int. Ed.* **55**, 7136–7141 (2016).

49. Wang, F. *et al.* A rechargeable aqueous Zn^{2+} -battery with high power density and a long cycle-life. *Energy Environ. Sci.* **11**, 3168–3175 (2018).

50. Kumar, S., Verma, V., Arora, H., Manalastas, W. & Srinivasan, M. Rechargeable Al-metal aqueous battery using NaMnHCF as a cathode: investigating role of coated-Al anode treatments for superior battery cycling performance. *ACS Appl. Energy Mater.* **3**, 8627-8635 (2020).

51. Zhang, Z. *et al.* Zeolitic Vanadomolybdates as High-Performance Cathode-Active Materials for Sodium-Ion Batteries. *ACS Appl. Mater. Interfaces* **12**, 6056–6063 (2020).

52. Liu, L., Wu, Y.-C., Rozier, P., Taberna, P.-L. & Simon, P. Ultrafast Synthesis of Calcium Vanadate for Superior Aqueous Calcium-Ion Battery. *Research* **6585686** (2019).

53. Park, C., Park, S. Bin, Oh, S. H., Jang, H. & Cho, W. Il. Li ion diffusivity and improved electrochemical performances of the carbon coated $LiFePO_4$. *Bull. Korean Chem. Soc* **32**, (2011).

54. Vujković, M., Stojković, I., Cvjetićanin, N. & Mentus, S. Gel-combustion synthesis of $LiFePO_4$/C composite with improved capacity retention in aerated aqueous electrolyte solution. *Electrochim. Acta* **92**, 248–256 (2013).

55. Rui, X. H., Yesibolati, N., Li, S. R., Yuan, C. C. & Chen, C. H. Determination of the chemical diffusion coefficient of Li^+ in intercalation-type $Li_3V_2(PO_4)_3$ anode material. *Solid State Ionics* **187**, 58–63 (2011).

56. Vujković, M., Mitrić, M. & Mentus, S. High-rate intercalation capability of $NaTi_2(PO_4)_3$/C composite in aqueous lithium and sodium nitrate solutions. *J. Power Sources* **288**, 176–186 (2015).

57. Ye, W. *et al.* Highly efficient lithium container based on non-Wadsley-Roth structure $Nb_{18}W_{16}O_{93}$ nanowires for electrochemical energy storage. *Electrochim. Acta* **292**, 331–338 (2018).

58. Agyeman, D. A., Song, K., Lee, G. H., Park, M. & Kang, Y. M. Carbon-Coated Si Nanoparticles Anchored between Reduced Graphene Oxides as an Extremely Reversible Anode Material for High Energy-Density Li-Ion Battery. *Adv. Energy Mater.* **6**, 1600904 (2016).

59. Zhang, L. *et al.* In Operando Mechanism Analysis on Nanocrystalline Silicon Anode Material for Reversible and Ultrafast Sodium Storage. *Adv. Mater.* **29**, 1604708 (2017).

60. Lee, Y. S. & Ryu, K. S. Study of the lithium diffusion properties and high rate performance of TiNb6O17 as an anode in lithium secondary battery. *Sci. Reports* **7**, 1–13 (2017).

61. Heubner, C., Schneider, M. & Michaelis, A. Investigation of charge transfer kinetics of Li-Intercalation in LiFePO4. *J. Power Sources* **288**, 115–120 (2015).

62. Yi, T. F. *et al.* Synthesis and application of a novel $Li_4Ti_5O_{12}$ composite as anode material with enhanced fast charge-discharge performance for lithium-ion battery. *Electrochim. Acta* **134**, 377–383 (2014).

63. Piao, T., Park, S., Doh, C. & Moon, S. Intercalation of Lithium Ions into Graphite Electrodes Studied by AC Impedance Measurements. *J. Electrochem. Soc.* **146**, 2794–2798 (1999).

64. Tang, K., Yu, X., Sun, J., Li, H. & Huang, X. Kinetic analysis on $LiFePO_4$ thin films by CV, GITT, and EIS. *Electrochim. Acta* **56**, 4869–4875 (2011).

65. Rui, X. H., Ding, N., Liu, J., Li, C. & Chen, C. H. Analysis of the chemical diffusion coefficient of lithium ions in $Li_3V_2(PO_4)_3$ cathode material. *Electrochim. Acta* **55**, 2384–2390 (2010).

66. Wan, L. F., Incorvati, J. T., Poeppelmeier, K. R. & Prendergast, D. Building a Fast Lane for Mg Diffusion in α-MoO_3 by Fluorine Doping. *Chem. Mater.* **28**, 6900–6908 (2016).

67. Koketsu, T. *et al.* Reversible magnesium and aluminium ions insertion in cation-deficient anatase TiO_2. *Nat. Mater.* **16**, 1142-1148 (2017).

68. Reddy, M. V. *et al.* Studies on the lithium ion diffusion coefficients of electrospun Nb_2O_5 nanostructures using galvanostatic intermittent titration and electrochemical impedance spectroscopy. *Electrochim. Acta* **128**, 198–202 (2014).

69. Wang, W. L., Park, J. Y., Nguyen, V. H., Jin, E. M. & Gu, H. B. Hierarchical mesoporous rutile TiO_2/C composite nanospheres as lithium-ion battery anode materials. *Ceram. Int.* **42**, 598–606 (2016).

70. Wunde, F., Berkemeier, F. & Schmitz, G. Lithium diffusion in sputter-deposited $Li_4Ti_5O_{12}$ thin films. *J. Power Sources* **215**, 109–115 (2012).

71. Han, C., Li, H., Li, Y., Zhu, J. & Zhi, C. Proton-assisted calcium-ion storage in aromatic organic molecular crystal with coplanar stacked structure. *Nat. Commun. 2021 121* **12**, 1–12 (2021).

Acknowledgements:

N.K. acknowledges funding support from the USA National Science Foundation (award numbers 1922633 and 2126178). NK also acknowledges funding support from the John A. Clark and Edward T. Crossan endowed Chair Professorship at the Rensselaer Polytechnic Institute.

Author Contribution:

A.S.L. designed and conducted the battery testing. A.S.L., K.B. and V.M. conducted materials synthesis. A.S.L., R.A.P. and S.S. contributed to materials characterization. A.S.L. and N. K. wrote the manuscript. N. K. supervised the research project and contributed to analyzing and interpreting the data. All authors discussed the results and commented on the manuscript.

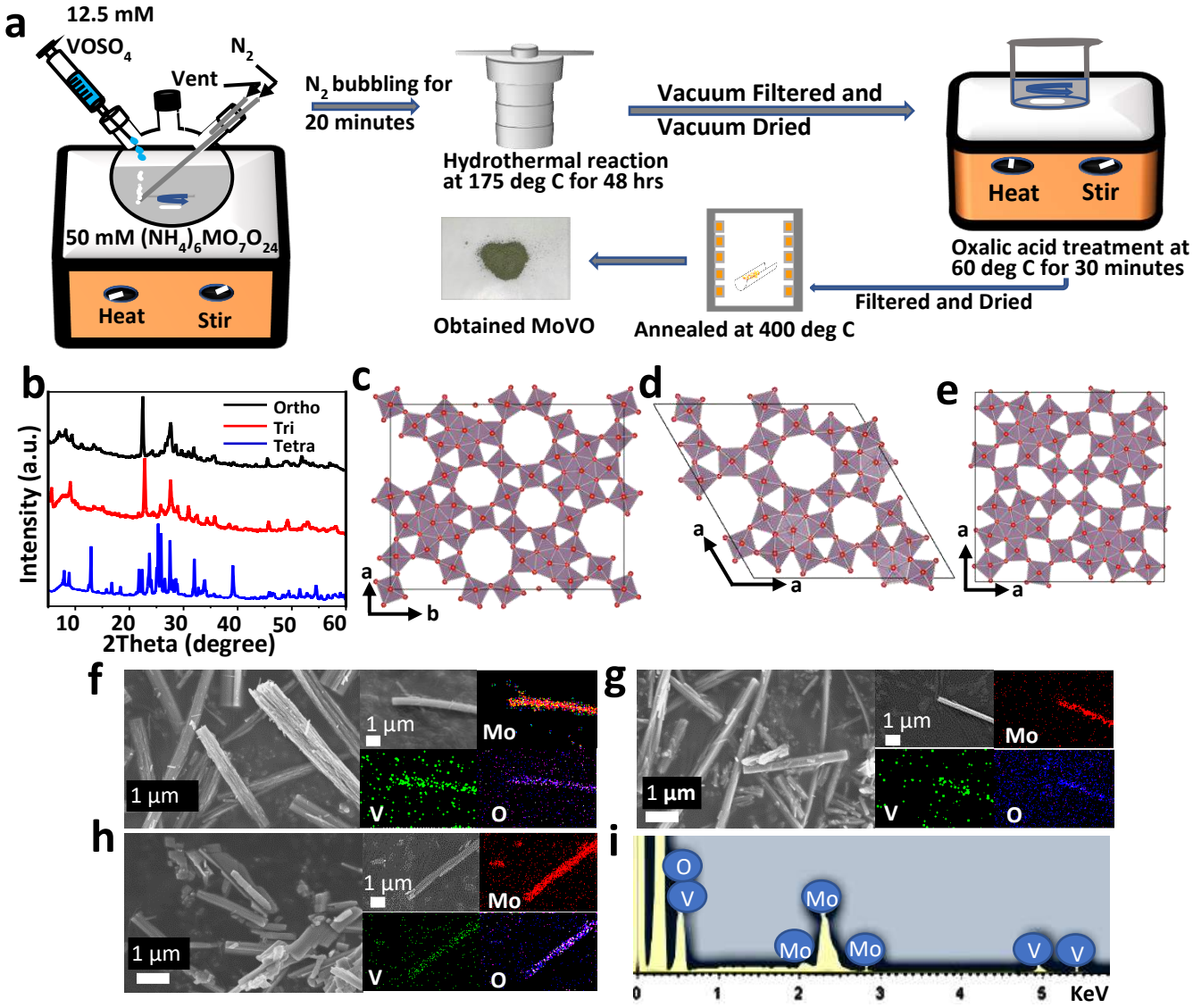

Figure 1 | Synthesis procedure, crystal structure and characterization of MoVO. a) Schematic of all steps involved in synthesis of Ortho MoVO. Tri MoVO synthesis involves pH adjustment (of precursor solution) to 2.2 using 2M H_2SO_4 and hydrothermal reaction for 20 hrs. Tetra MoVO was obtained by annealing Ortho MoVO at 575 ^{0}C under N_2 atmosphere. **b)** XRD result of all three MoVO compounds. Crystal structure of **c)** Otho **d)** Tri and **e)** Tetra MoVO. Orthorhombic and trigonal structure contains hexagonal and heptagonal tunnels, whereas tetragonal polymorph contains pentagonal, tetragonal and trigonal tunnels. SEM images and EDS mapping of synthesized rods of **f)** Ortho **g)** Tri and **h)** Tetra MoVO. Mapping shows distribution of Mo, V and O throughout the rod. **i)** EDS spectrum of Tri MoVO. Ortho and Tetra spectrum also exhibit similar peaks for Mo, V and O.

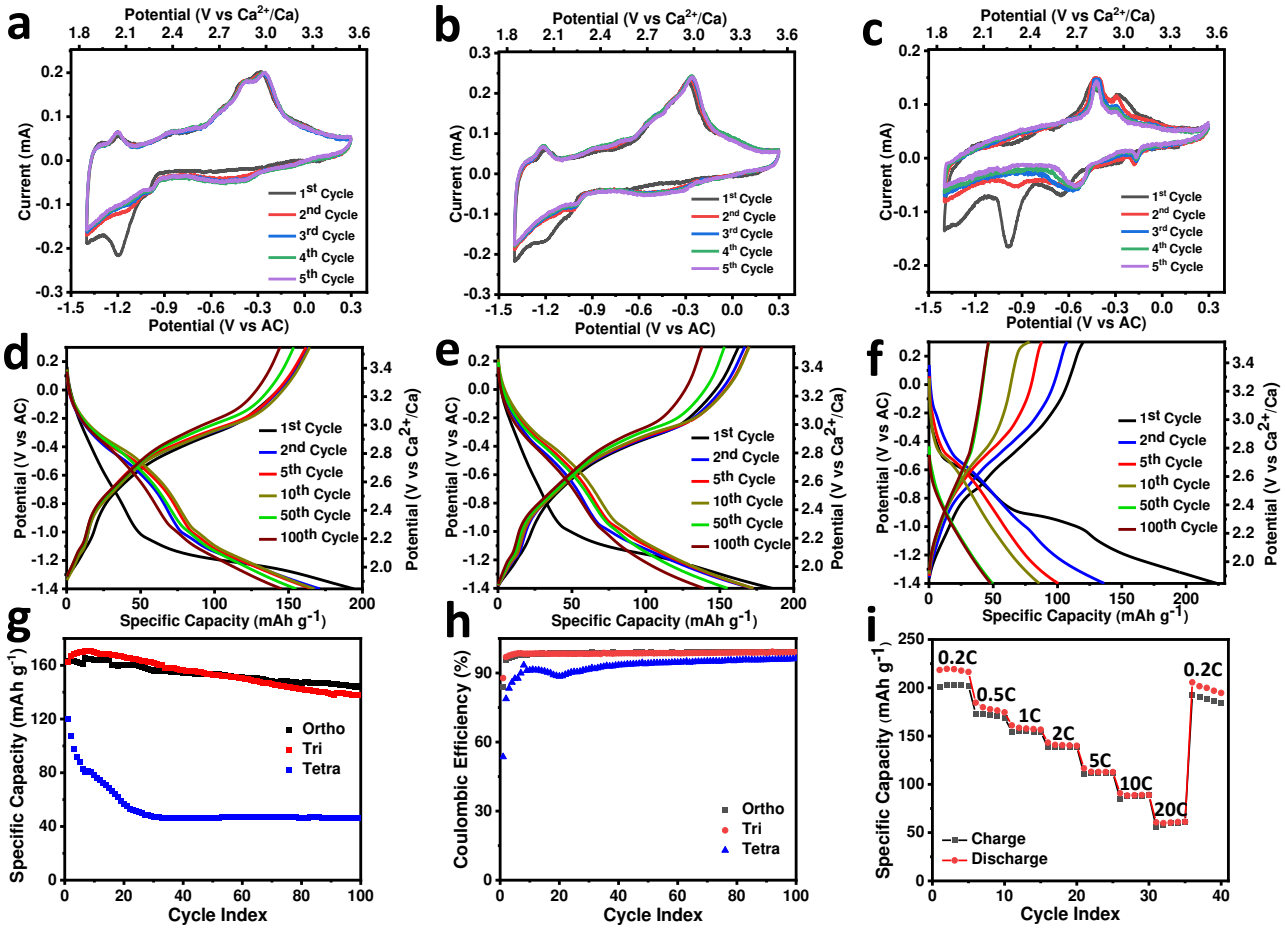

Figure 2 | Electrochemical performance of MoVO compounds in a Ca-ion battery. Cyclic voltammetry results of **a)** Ortho, **b)** Tri and **c)** Tetra MoVO performed at 0.1 mv s^{-1}. Five cycles were performed to get a reversible CV profile. Voltage profile acquired using galvanostatic test at 100 mA g^{-1} for **d)** Ortho, **e)** Tri and **f)** Tetra MoVO. **g)** Comparison of cyclic stability over 100 cycles among all three polymorphs of MoVO. **h)** Coulombic efficiency over 100 cycles, revealing high reversibility of Ortho and Tri over Tetra MoVO. **i)** Rate capability test of Tri MoVO (1C = 150 mA g^{-1}). Five cycles were performed at each rate to establish stable performance of the compound.

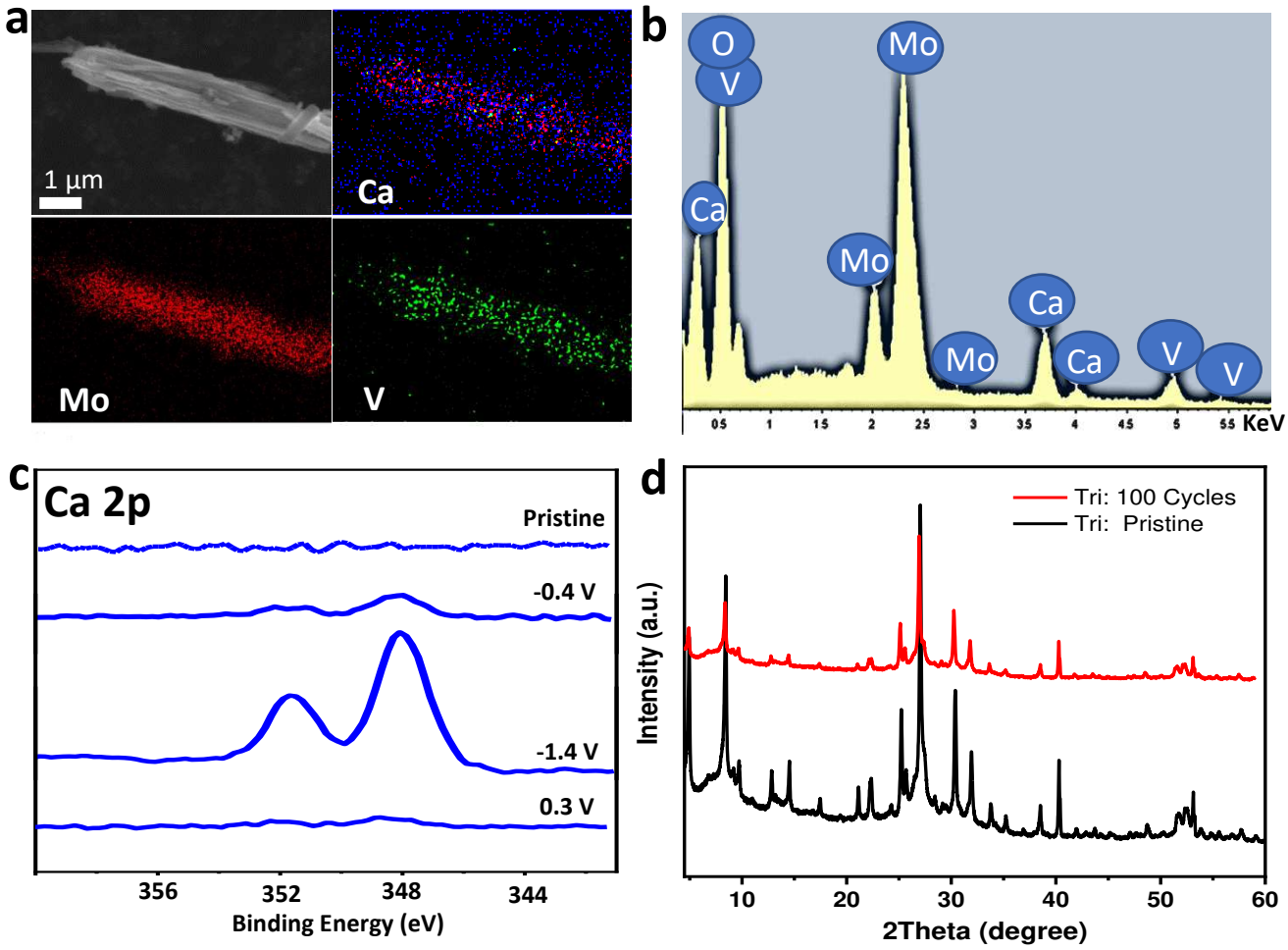

Figure 3 | Ex-situ EDS, XPS and XRD of Tri MoVO. **a)** Ex-situ EDS of Tri MoVO at final discharge state of -1.4 V. Uniform distribution of calcium is quite visible in the mapping. **b)** EDS spectrum of this electrode also show peaks corresponding to Ca, Mo, V and O. This confirms that calcium inserts inside the material. **c)** Ex situ XPS spectrum of Ca at different voltages during the discharge cycle. Ex-situ study was performed on pristine electrodes, at discharge potential of -0.4 V, complete discharge at -1.4 V and finally complete charge at 0.3 V. The appearance of Ca 2p peak during discharge and disappearance at charge shows high Ca reversibility during the battery cycling process. **d)** Comparison of XRD profile of pristine Tri MoVO electrode and Tri MoVO electrode tested in the battery for 100 cycles. The electrode maintains the same XRD profile, validating the fact that the crystal structure of the material is preserved during cycling.

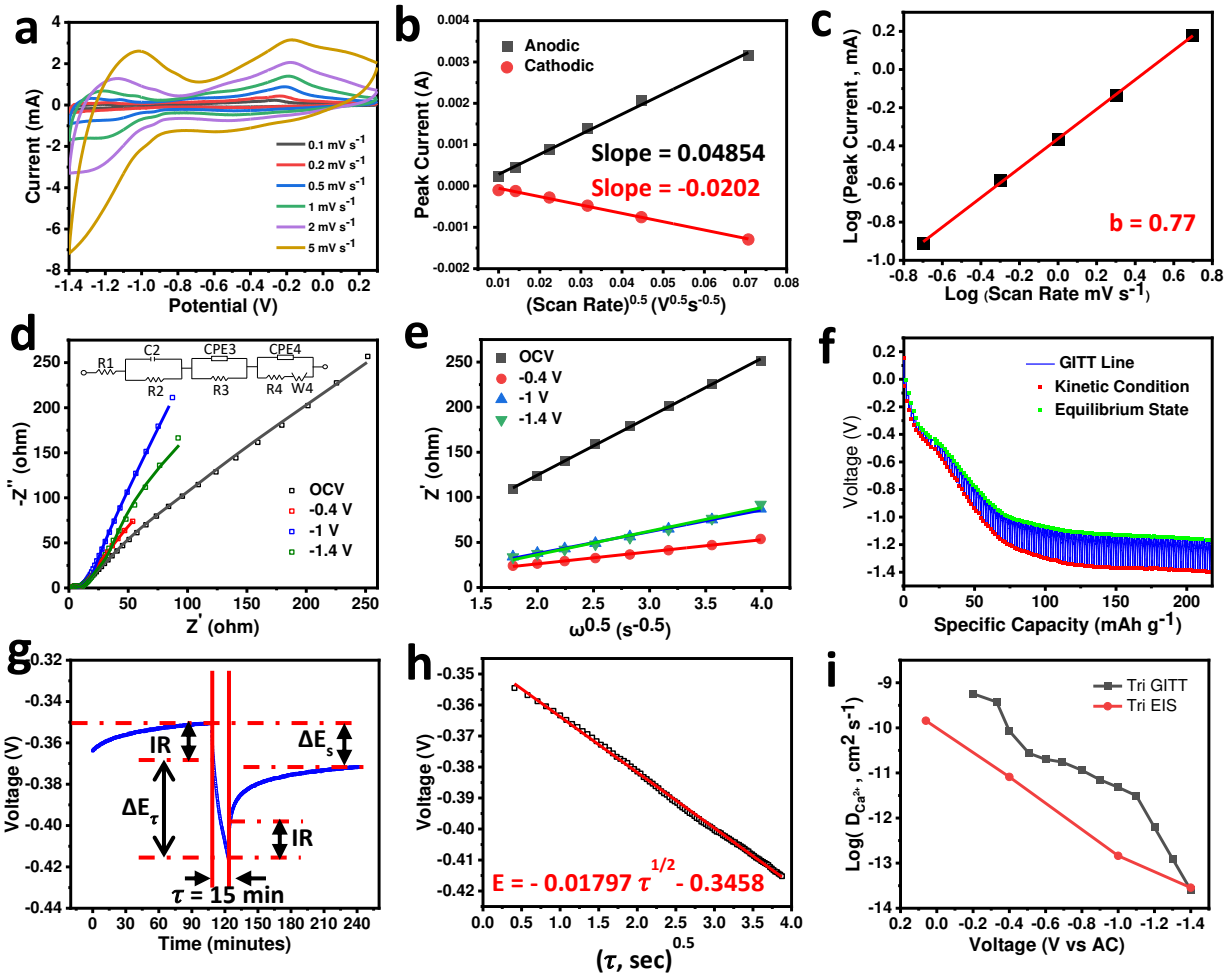

Figure 4 | Diffusion coefficient calculation of Ca^{2+} in Tri MoVO. a) Cyclic Voltammetry at different sweep rates. **b)** Linear fit of peak current vs (scan rate)$^{0.5}$ at -0.27 V (anodic) and -0.51 V (cathodic) potential. The slope from these plots were used to calculate diffusion coefficient using the Randles-Sevcik model. **c)** Power law relation between peak current and scan rate at -1.22 V. 'b' value of 0.77 suggests that the storage mechanism contains both diffusive and capacitive contribution and that the Randles-Sevcik equation cannot be applied here. **d)** EIS of Tri MoVO at different voltage values during the discharge process. Inset shows the model used to fit the data. **e)** Z' (real part of impedance) vs $\omega^{0.5}$ at low frequency regime of EIS. Warburg factor (σ) was obtained from the slope to calculate the diffusion coefficient. **f)** Discharge GITT curve of Tri MoVO. **g)** Zoomed in plot of GITT curve at approximately -0.4 V. Current pulse (τ) 0f 15 min was applied with 2 hrs. of relaxation time. **h)** Voltage vs $\tau^{0.5}$ at -0.4 V shows linear relation. **i)** Calculated Ca^{2+} diffusion coefficient values using EIS and GITT at different voltage values.

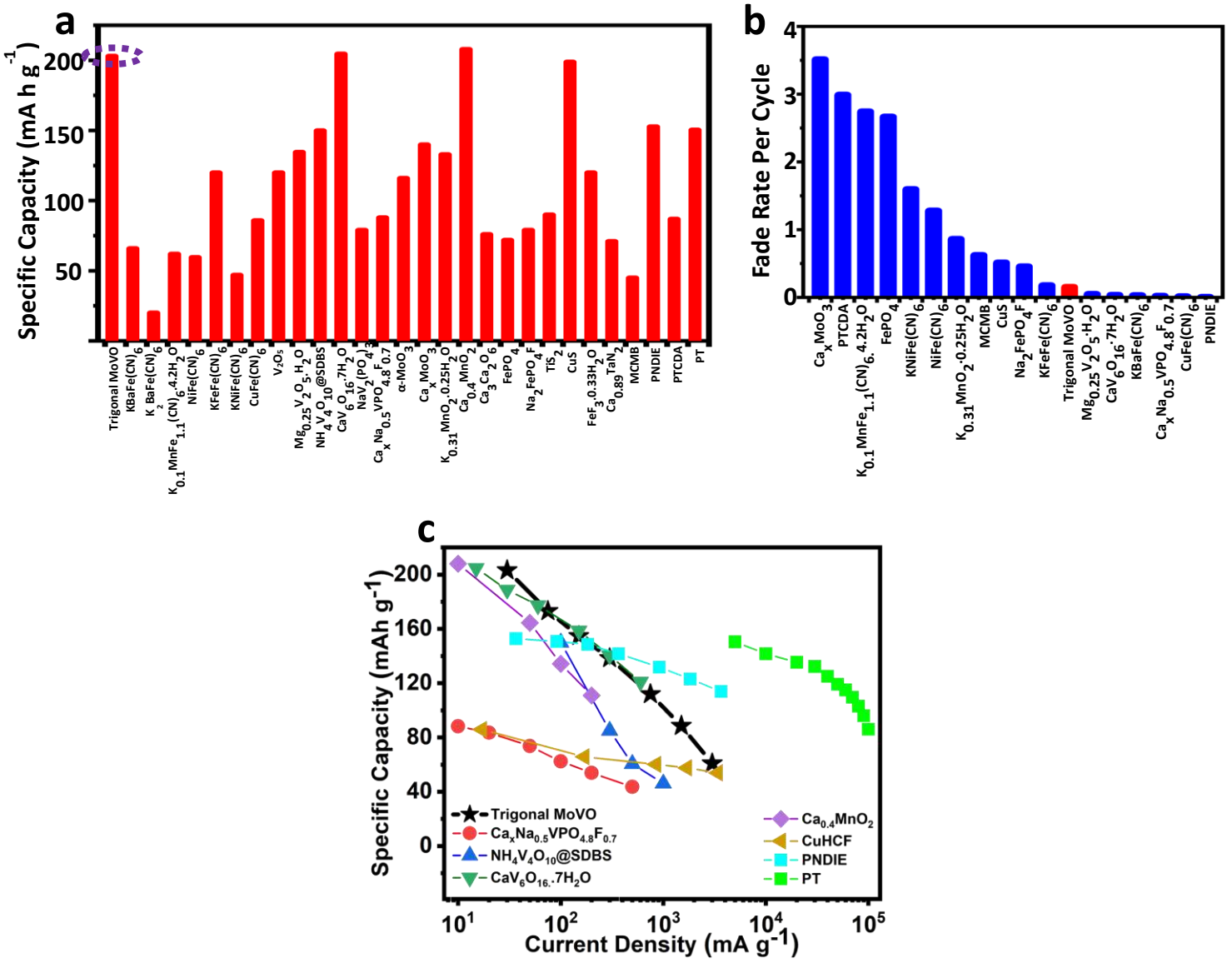

Figure 5 | Tri MoVO performance comparison with the literature for Ca-ion batteries. a) Specific capacity of Tri MoVO compared with reported materials employed in Ca-ion batteries (refer to the Supplementary Table 1 for full details). Abbreviations for SDBS: sodium dodecylbenzenesulfonate, MCMB: mesocarbon microbeads, PNDIE: poly[N,N′-(ethane-1,2-diyl)-1,4,5,8-naphthalenetetracarboxiimide,PTCDA: Perylene-3,4,9,10-tetracarboxylic dianhydride , and PT: 5,7,12,14-pentacenetetrone.**b)** Percentage fade rate per cycle of various materials tested in Ca-ion batteries. Literature showing cyclic stability results were used to generate the plot. Some articles showing negative fade rate are not shown here but mentioned in the Supplementary Table 1. **c)** Specific capacity vs current density. Articles reporting rate performance of the material have been displayed.

Supplementary Files

This is a list of supplementary files associated with this preprint. Click to download.

- SupplementaryFile.pdf